Flow field in fouling spiral wound reverse osmosis membrane modules using MRI velocimetry

Bristow, Nicholas W.; Vogt, Sarah J.; O'Neill, Keelan T.; Vrouwenvelder, Johannes S.; Johns, Michael L.; Fridjonsson, Einar O.

DOI
10.1016/j.desal.2020.114508

Publication date
2020

Document Version
Final published version

Published in
Desalination

Citation (APA)
Bristow, N. W., Vogt, S. J., O'Neill, K. T., Vrouwenvelder, J. S., Johns, M. L., & Fridjonsson, E. O. (2020). Flow field in fouling spiral wound reverse osmosis membrane modules using MRI velocimetry. *Desalination*, *491*, Article 114508. https://doi.org/10.1016/j.desal.2020.114508

Desalination 491 (2020) 114508

Contents lists available at ScienceDirect

Desalination

journal homepage: www.elsevier.com/locate/desal

Flow field in fouling spiral wound reverse osmosis membrane modules using MRI velocimetry

Nicholas W. Bristow[a], Sarah J. Vogt[a], Keelan T. O'Neill[a], Johannes S. Vrouwenvelder[b,c], Michael L. Johns[a], Einar O. Fridjonsson[a,*]

[a] Department of Chemical Engineering, The University of Western Australia, Crawley, WA 6009, Australia
[b] Biological and Environmental Sciences and Engineering Division, Water Desalination and Reuse Center, King Abdullah University of Science and Technology, Thuwal 23955-6900, Saudi Arabia
[c] Department of Biotechnology, Faculty of Applied Sciences, Delft University of Technology, Van der Maasweg 9, 2629 HZ, Delft, the Netherlands

ARTICLE INFO

Keywords:
Biofouling
MRI
Imaging
Velocity mapping
Drinking water production

ABSTRACT

Magnetic Resonance Imaging (MRI) velocimetry was applied to study non-invasively the water flow field inside a spiral-wound desalination membrane module (diameter: 2.5 in.; length: 18.5 in.), located in a pressure vessel, at typical practice operational conditions as a function of alginate fouling, simulating extracellular polymeric substances (EPS). Cross-sectional velocity images were acquired at an in-plane spatial resolution of 0.137 mm at multiple locations along the length of the reverse osmosis module and were acquired as a function of alginate concentration. At a total system alginate concentration of 3.25 mg/l, significant changes in the cross-sectional velocity map were observed near the module inlet due to alginate fouling, with limited changes observed in the middle and outlet regions of the module. When the total system alginate concentration was increased to 75 mg/l, it caused the module brine seal to fail resulting in significant local water flow by-passing the membrane module. This was clearly discernible in this opaque membrane system using MRI and resulting in dramatic changes in fluid velocity distribution through the membrane module. These observations of significant flow field heterogeneity as fouling develops are consistent with 'irreversible' fouling effects noted frequently in practice by the water treatment industry.

1. Introduction and background

Highly populated areas and arid zones around the world suffer from vulnerability to limited clean freshwater availability; these water sources will need to be supplemented in order to meet the projected increase in consumption [1]. Reverse osmosis (RO) membrane technology has developed over the past 40 years to account for 80% of the total desalination plants installed worldwide with strong growth projections [2,3]. Membrane fouling, particularly biofouling, is a major concern for the desalination industry [4–8], as it decreases membrane performance and shortens the membrane lifespan, posing an economic burden on plant operations estimated at up to 25–50% of total plant operating costs [9,10] as well as in worst cases posing a risk for the reliability of (drinking) water supply. Such biofouling cannot be solved by pre-treatment of the water alone [11–13], this is attributed to biofilm formation on membrane and feed-channel spacer sheet surfaces within the spiral wound membrane modules, which once established are capable of rapid re-emergence even after intensive and repetitive chemical cleaning treatment [14].

Biofilms are an accumulation of micro-organisms and extracellular material which forms a matrix which can be irreversibly bonded onto the membrane and/or feed spacer surface, with the main mechanism for cohesion and adhesion of the biofilm matrix due to extracellular polymeric substances (EPS) which contributes up to 80% of the organic matter [15,16]. EPS is primarily composed of polysaccharides, proteins and other macro-molecules and functions to improve adhesion to surfaces, improve resistance to antimicrobial substances and chemical biocides and sequesters ions from the feed water to feed the bacterial colony. This biofilm growth inhibits convective transport locally [17,18], which causes a back-bone (or telescoping) flow regime to emerge [19–21] with substantial loss of membrane performance. Vrouwenvelder et al. [22] showed that biofilm accumulation in RO membrane elements increases the feed side pressure drop between the inlet and the more concentrated discharge outlet of the module (hereafter referred to as the feed-channel pressure drop); both direct observation [23] and impedance spectroscopy [24] have been used to

* Corresponding author.
E-mail address: einar.fridjonsson@uwa.edu.au (E.O. Fridjonsson).

https://doi.org/10.1016/j.desal.2020.114508
Received 6 February 2020; Received in revised form 4 May 2020; Accepted 5 May 2020

characterise such fouling. A membrane fouling simulator (MFS) can also be operated in parallel to the actual RO membrane system [11], previous research [10] has found that the MFS closely mimic the biofouling effects inside the RO membrane modules.

In this work alginate, a long chain polysaccharide, is used to simulate the physical properties of extracellular polymeric substances (EPS). There is significant precedent in the use of alginate as an EPS substitute in membrane biofouling studies and the conditions for alginate fouling are well defined [25–27], these studies examined the effect of different chemical and hydrodynamic parameters on permeate flux. Van den Brink et al. [28] identified that calcium and magnesium form 'bridging' bonds in alginate compounds and then examined the impact of calcium ion concentration on membrane fouling using alginate compounds. They found that high concentrations of calcium led to higher fouling rates, whilst high concentrations of ionic strength (sodium concentration) served as an inhibitor. These results collectively support the use of alginate as a controllable model foulant to mimic the effects of biological fouling, allowing for systematic and reproducible studies of RO membrane fouling processes. Whilst alginate fouling does not necessarily share the same initial growth phases as biofouling, once biofouling is established it does lead to the accumulation of EPS rich material at spacer-nodes and on membrane which can be mimicked by the use of alginate [29].

The flow field within a spiral wound (SW) reverse osmosis (RO) membrane module is engineered to give support to the membrane leaves, as well as produce sufficient mixing and cross-flow over the membrane surface so as to minimise concentration polarisation (CP) and fluid hold-up on the feed side [30]. The introduction of stationary foulants into a membrane system causes localised flow resistance, disrupting the local and downstream flow field which can result in an increase of both CP and fluid hold-up. To this end we seek to directly visualise and quantify this flow disruption using Magnetic Resonance Imaging Velocimetry. The subsequent analysis of the spatial velocity distributions allows new insight into the flow field through both an unfouled and fouled spiral wound membrane module in a pressure vessel.

MRI has the unique ability to non-invasively measure flow fields within opaque porous media without adding tracers and has previously been used to characterise velocity in both commercial hollow fiber and spiral wound membranes. Pangrle et al. [31] applied MRI velocimetry to identify flow distributions in a hollow fiber membrane. This work has been expanded and extended upon significantly to observe hollow fiber membranes' fouling and operational phenomena in various configurations such as hemodialyzers and membrane bioreactors [32–41]. The first application of MRI and velocity imaging of biologically fouled spiral wound membranes was by Graf von der Schulenburg et al. [42]. This showed spatially resolved biological material fouling of the feed spacer and membrane and illustrated the formation of preferential flow paths through the membrane module. Limitations of this research were that the permeate tube was isolated during both fouling and MRI analysis and that membrane cross flow was only 0.2 cm/s during MRI analysis. In corresponding smaller scale membrane fouling simulator (MFS) MRI velocity measurements, preferential 'backbone' flow was observed through the feed spacer. This MRI work was expanded upon by Vrouwenvelder et al. [22] where it was observed that biofouling has an affinity for the feed spacer which significantly impacted overall water flow distribution in the spiral wound membranes; this was confirmed via autopsied membranes. Evaluation of the impact of chemical cleaning by Creber et al. [43] determined that the formation of preferential flow channels through the membrane modules meant that the applied cleaning regimes were largely ineffective and consequently once the biofouling was established, it was extremely difficult to remove. Low cost low field (LF) NMR has also more recently been used to examine SWRO membrane modules [44–46]. It was found that results from the LF-NMR were comparable to high field MRI results, demonstrating that statistical analysis of the NMR signal could be used to detect flow aberrations due to biological fouling on the feed spacer earlier than detected by sensitive differential pressure measurements [44,46].

This study aims to measure the flow velocity field before and after fouling at close to realistic operational flow conditions by operating at the lower operating limits of the commercial SWRO membrane module in a pressure vessel. Axial and radial changes in the velocity flow field are non-invasively determined to assess the impact of the fouling on the overall flow field across the module, resulting in new insights regards the effect of fouling on the overall module. In the current experimental study, the fouling of SWRO membranes is investigated at an order of magnitude higher volumetric crossflow rates (Q = 60 L/h; cross flow velocity ≈ 2 cm/s) than previous biofouling in SWRO MRI research [42] and thus at more industrially relevant flow velocities. We use sodium-alginate as a biofouling substitute to produce controlled and reproducible fouling effects within a small scale (2.5 in. diameter, 18.5 in. length) commercial SWRO membrane module. The impact of fouling on the membrane is examined at three axial locations (inlet (1.5 in. from start of membrane), middle (9-inch from start of membrane) and outlet (1.5 in. from end of membrane)) to ascertain the impact of fouling on the flow through the membrane module. The flow field is monitored using velocity-encoded magnetic resonance imaging (MRI) [47], which allows for non-invasive and non-destructive monitoring of the velocity field within a commercial membrane pressure housing.

2. Methodology

2.1. Membrane flow loop setup

Fig. 1(a) shows a schematic of the membrane flow loop used for the fouling operation. The membrane module was operated in water recirculation mode comprised of a feed tank containing 30 l, with permeate and concentrate lines returned to the feed tank. The RO membrane module was installed in a commercially available pressure vessel (PV-2521-SW, Hydrocomponents Technology Industries, CA, USA). The pressure vessel was fitted with custom machined nylon components (Fig. 1(c)) to replace aluminium endcap retainers to allow installation in the MRI system. Nylon retainers were pressure tested up to 40 bar and proved suitable for the expected pressure ranges when membrane crossflow would be maintained at 60 l/h at a pressure of 20 bar. The membrane module used for this work was a commercially available DOW Filmtec XLE 2521 module. The membrane surface has been previously defined [48] as: molecular weight cut off: 100 Da; Contact angle: 66.3° and zeta potential: −2.5 mV (pH 6 in 0.01 M NaCl solution). The membrane was prepared prior to fouling operations through flushing with 500 l of RO permeate (< 2 μS/cm) for approximately 2 h to flush any unreacted polymer and other impurities from the membrane module as recommended by DOW [49]. All membrane discharge lines (permeate and concentrate) were directed to drain during this operation. Differential pressure across the membrane/pressure vessel assembly was monitored using an Endress+Hauser PMP131-A2501Q4S 400 pressure gauge and the membrane permeate and concentrate discharge flowrates were monitored using suitable range rotameters (Stubbe DFM165 5–60 l/h and DFM350 30–300 l/h respectively).

The fouling material was a medium molecular weight sodium alginate, Manugel GMB alginate (FMC Biopolymer) and was prepared as 1 g/l solution in deionised water. A salt solution containing 1 g/l NaCl and 0.7 g/l $CaCl_2$ was initially circulated in the membrane flow loop at 60 l/h and MRI velocity images were acquired. Small dosages (25 ml) of the alginate solution were then introduced to the pump suction of pump (Fig. 1(a)) until the total system alginate concentration equalled 3.25 mg/l. The system was then flushed at 400 l/h for 2 h to dislodge any loose material in the system. The system was allowed to stabilise before MRI velocity measurements were acquired at the module inlet, middle and outlet respectively. The system alginate concentration was then gradually increased to 75 mg/l, followed by a stabilisation period

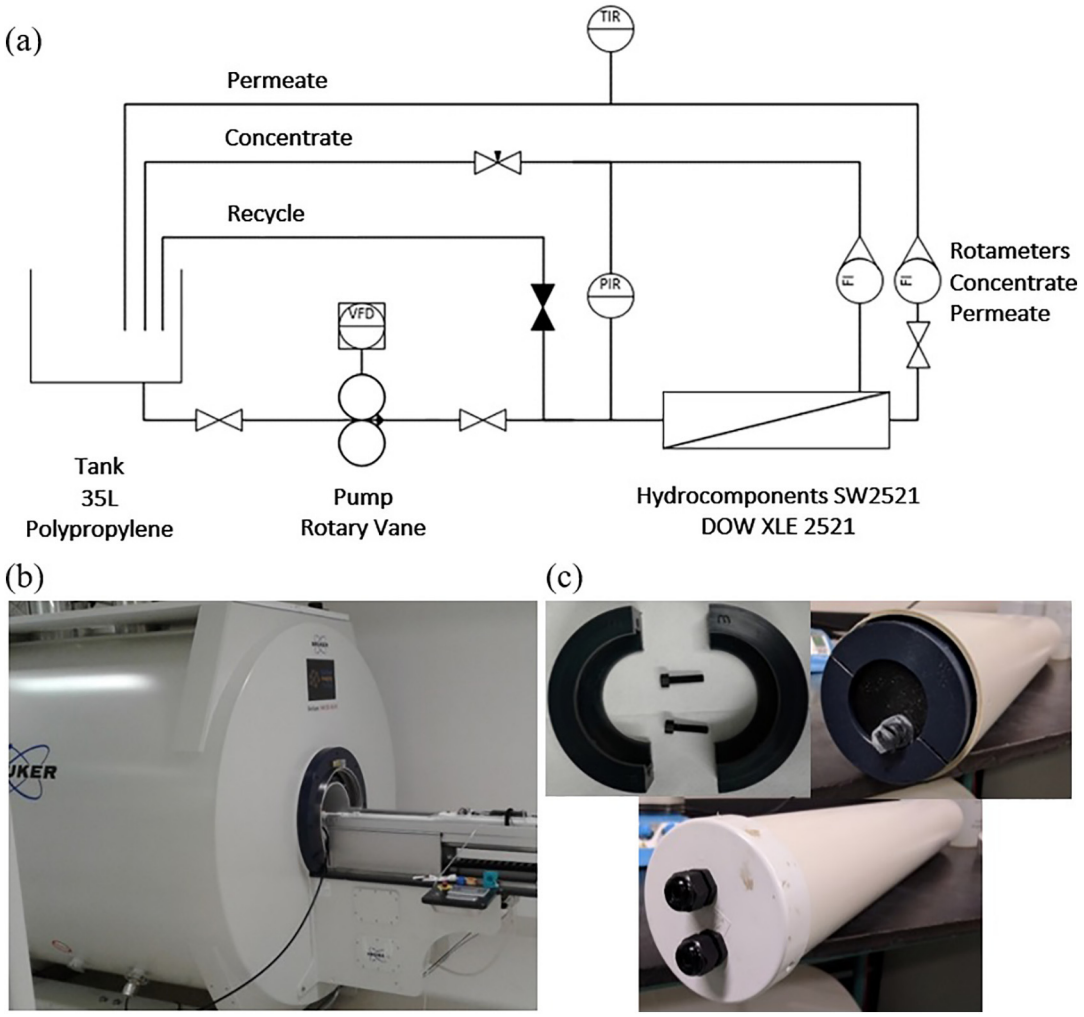

Fig. 1. (a) Process flow diagram schematic of the flow loop used in this study; (b) a Bruker BioSpec 9.4 T Magnetic Resonance Imaging (MRI) into which the pressure vessel containing the membrane module was placed; (c) custom made nylon end-caps retainers to seal the feed-side of the reverse osmosis (RO) membrane module and their assembly into the pressure vessel.

of 2 h at 60 l/h, before the MRI velocimetry measurements were repeated.

2.2. MRI equipment & imaging protocols

The MRI system used in this study was a Bruker BioSpec 9.4 T MRI with a Bruker Avance III digital RF system with 8-channel transmit/receive capability (Fig. 1(b)), using a 20 cm internal diameter imaging gradient set (maximum gradient of 0.3 T/m) and a 154 mm ^{1}H RF coil. The MRI pulse sequence used for velocity images is a FLASH imaging sequence with flow compensation of the imaging gradients in three directions and with velocity phase encoding gradients in the slice direction (as shown in Fig. 2). To produce each velocity image two phase-encoded images are acquired: one image with a positive velocity encoding gradient and one image with an equal and opposite (negative) velocity encoding gradient. The phase difference of each imaging voxel is then linearly related to the velocity of the fluid, U:

$$U = \frac{\Delta\theta}{2\gamma\delta g} \tag{1}$$

where $\Delta\theta$ is the measured phase difference in radians; γ is the gyromagnetic ratio (for ^{1}H in this case); δ is the velocity encoding gradient duration and g is the velocity encoding gradient strength. The acquisition of the positive and negative velocity images are interleaved, hence both are being acquired over the full experimental time. The imaging parameters for each image are 512 by 512 voxels (=262,144 voxels) over a cross-sectional 70 mm by 70 mm field of view (an in-plane resolution of 0.137 mm which corresponds to on average 6 voxels across feed channel) and a 2.5 mm slice thickness. The echo time (T_E) used was 7.08 ms, δ was 3.24 ms and g was 1.47 mT/m. The total experimental acquisition time for a velocity image was 1 h 50 min.

2.3. MRI velocity image analysis

Fig. 3(a) shows a standard MRI image of a cross-section of the membrane when the fluid content is stationary (no fluid flow). The central permeate channel is immediately evident as is the water-containing gap between the membrane module and the inner wall of the pressure vessel. Given that the fluid is stationary, air has accumulated at the top of this gap. The membrane sheets are evident in the intermediate region; greater signal is detected from the spacers between the membrane sheets and reflects the greater water content in these regions. The spiral assembly is composed of two interleaved membrane sheets (separated by spacers) which are wrapped multiple times around the central permeate channel. In order to determine the feed side velocity as a function of radial position (spiral number), the following image analysis was performed. Spiral profiles were fit to each of two interleaved membrane sheet, this was achieved using a logarithmic spiral [50], given in polar coordinates for a spiral radius (r) and angular coordinate (θ):

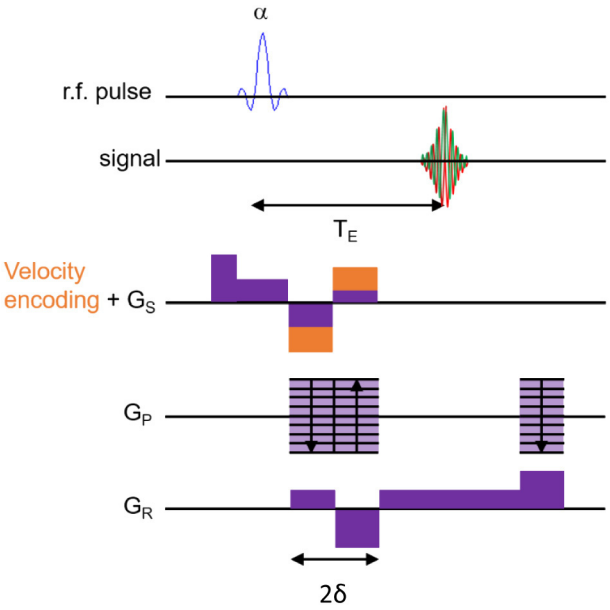

Fig. 2. Pulse sequence for FLASH imaging with flow compensation in all imaging directions (Gs, Gp, G_R) and velocity encoding in the slice direction (Gs). Imaging parameters: 512 × 512 pixels, 70 mm × 70 mm field of view; 2.5 mm slice thickness; T_E = 7.08 ms; Velocity encoding duration (2δ) = 3.24 ms; velocity encoding gradient = 1.47 mT/m; radiofrequency (r.f.) excitation pulse α = 30°; T_R = 50 ms; total experimental time 1 h 50 min.

$$r = ae^{\theta \cot(b)} \tag{2}$$

where *a* and *b* are the magnitude and angular parameters of the spiral. A logarithmic spiral was used due to slight asymmetry of the real spiral membrane module. Eq. (2) is solved for all rotations of the membrane sheets; a sample fit is shown for a velocity image in Fig. 3(b). This enables the mean velocity (and its standard deviation) in each 360° spiral to be readily determined for each of the two membrane sheets.

3. Results and discussion

The results of MRI velocity images for three locations (inlet, middle and outlet of the membrane module) are shown in Figs. 4 and 5 for the initial two fouling scenarios: 0 g/l of alginate (hereafter referred to as un-fouled) and 3.25 mg/l of alginate solution (hereafter referred to as lightly fouled). The un-fouled scenario (Fig. 4) corresponded to a feed channel pressure drop of 0.20 bar at a volumetric flowrate of 60 l/h. The lightly fouling scenario (Fig. 5) resulted in only a very modest increase in feed channel pressure drop from 0.20 to 0.37 bar at 60 L/h. In Fig. 4(d-f), counter-current flow (negative velocity) is immediately evident in the permeate tube and correctly increases towards the feed-side entrance. The measured mean velocity at the inlet location in the feed spacer filled channels is 2.40 cm/s, with a variance of 0.50 cm^2/s^2. Fig. 4(d-f) show cross-sectional velocity profiles across the corresponding images, whilst Fig. 4(g-h) shows the probability distribution of fluid velocity in the images for the feed channels. Despite this being a nominally clean membrane, a limited degree of velocity heterogeneity over the module length is evident. Limited stagnant zones are evident both towards the entrance and exit of the membrane module; these we speculate are partially a consequence of some compression of the membrane in these two zones as part of the module outer retainer sealing. Nevertheless, Gaussian shaped probably distributions of fluid velocity are produced for both these locations (Fig. 4(g) and (i)), which is consistent with well mixed flow. Whilst the middle of the membrane module appears visually to be more homogeneous in terms of velocity distribution, its probability distribution of velocity (Fig. 4(h)) presents two distinct peaks – this was reproducible across multiple membrane

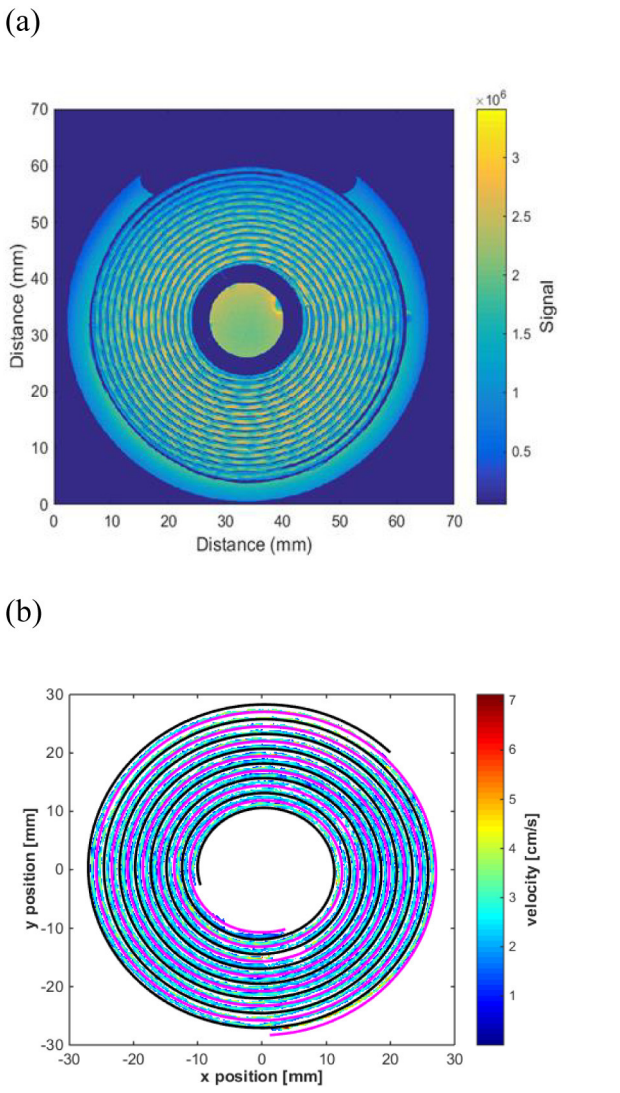

Fig. 3. (a) Conventional 2D MRI image of the membrane module in the pressure vessel assembly, containing water without fluid flow. The central permeate tube and the free space between the membrane module and in the inner wall of the pressure vessel are immediately obvious. The intermediate region of the image consists of two interwoven membrane sheets (with associated permeate and feed channel spacers) which are wound around the central permeate channel. (b) Membrane sheet spiral profiles at both sides of the feed spacer masking a velocity MRI sample image where the permeate channel and free space fluid signal have been masked out.

and flowrates, the reason for this we speculate is slightly lower compression of the membrane in this region resulting in slightly thicker feed spacer channels in which the velocity distribution is better resolved by the MRI images (this results in a lower mean velocity in the middle, compared with at the inlet and outlet (see Fig. 4(g-i))) – note the slightly thicker, on average, spirals evident in Fig. 4(b).

For the lightly fouled membrane module (Fig. 5), the mean velocity is 2.32 cm/s with a variance of 2.34 cm^2/s^2 at the inlet location, much larger than the case for the unfouled membrane module (0.50 cm^2/s^2). Greater variation in the spatial velocity distribution is immediately obvious in Fig. 5(a)-(c) relative to Fig. 4(a)-(c) and is attributed to alginate fouling causing a significant disruption to the flow field as reported previously for biofouled membrane modules [42,43]. Alginate was visually evident to have accumulated on the feed spacer sheets at the entrance to the membrane module when the system was autopsied post-imaging. The distribution is arguably greatest at the membrane entrance (Fig. 5(a)) where the oscillations in velocity (best viewed in

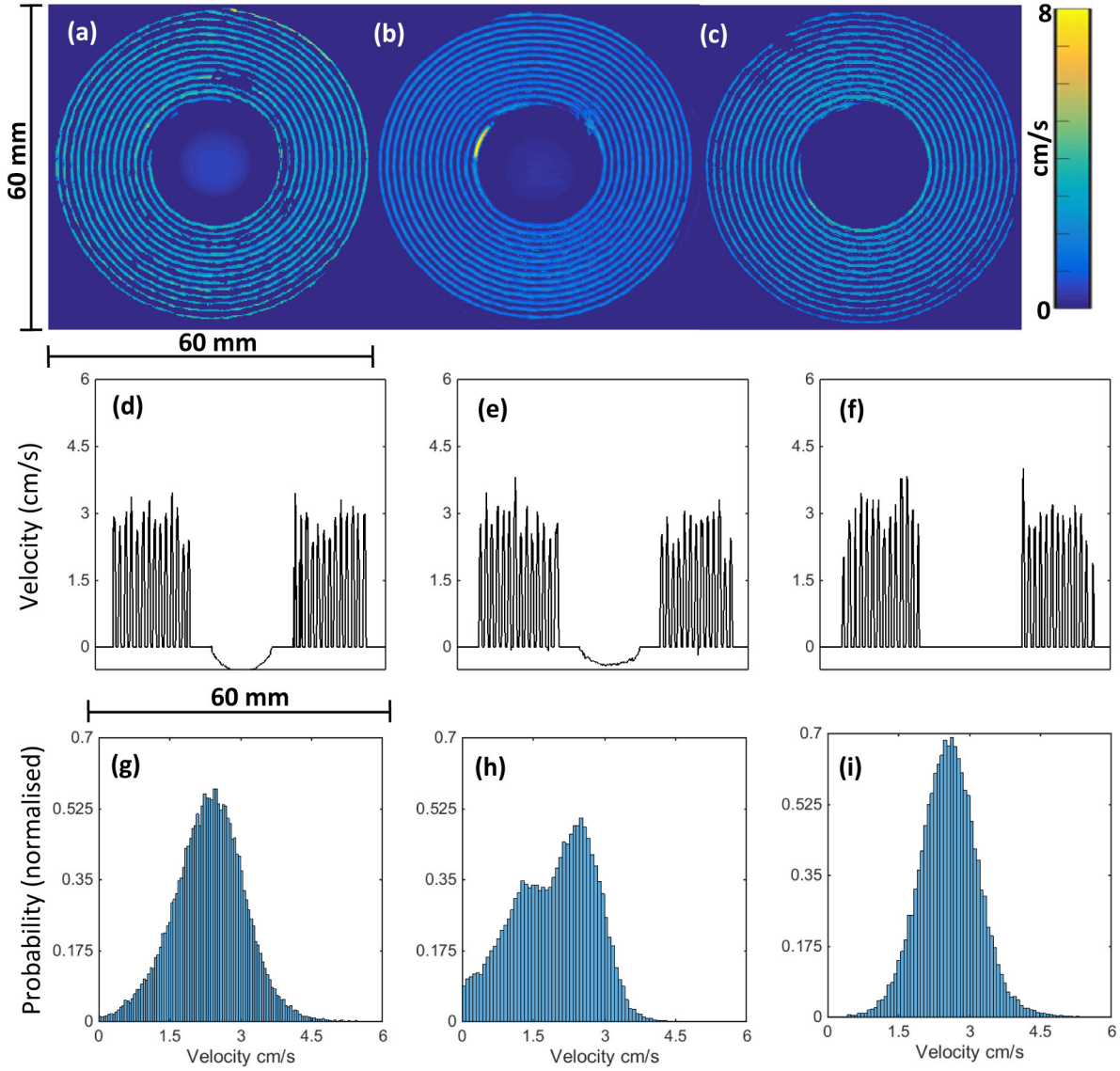

Fig. 4. Membrane exposed to no alginate fouling load (un-fouled scenario). Velocity images at (a) inlet, (b) middle and (c) outlet regions of the membrane module. Velocity profiles extracted from the mid-section of the velocity images are shown at the (d) inlet, (e) middle and (f) outlet regions. Histograms of the velocity distributions for the un-fouled membrane module at the (g) inlet, (h) middle and (i) outlet regions for the feed channels. Note: The area of high velocity next to the permeate pipe (Fig. 4b), is flow channelling due to the construction of the membrane module and the local partial absence of the feed spacer sheet.

Fig. 5(d)) indicate a greater influence on one of the two interleaved feed spacer sheets. For the middle and exit locations of the module, larger regions of stagnation are evident and a general decrease in velocity is observed as a function of radial position (in Fig. 5(e) and (f)). In both cases the probability distributions of velocity become distinctly less symmetric. Permeate production for the lightly fouled module is also clearly reduced (30%) relative to the clean membrane module despite the same water salt content being present in both measurements (the measured velocity distribution inside the permeate channel resulted in a permeate reduction from 1.25 l/m^{2}h (clean) to 0.83 l/m^{2}h (lightly fouled)).

With respect to the heavy fouling scenario where the system alginate concentration was increased to 75 mg/l, the feed side pressure drop was observed to initially increase from 0.37 bar to 2 bar after which it fluctuated between 1 and 2 bar. This resulted in severely distorted velocity images, a sample of which is shown in Fig. 6(a) for the entrance region of the membrane module – significant velocity heterogeneity is evident in this location with a significant portion of the image exceeding the dynamic range of the measurement (8 cm/s) and very limited permeate production being produced. More interestingly is the velocity map presented in Fig. 6(b) for the exit region of the membrane module. Here a clear non-zero velocity is measured for the gap between the module and the inner wall of the pressure housing with 76% of the flow by-passing the membrane module. This is a consequence of the brine seal on the outside of the module failing (confirmed upon system demobilisation) resulting in significant by-passing of the flow from the module into this region. Arguably such an effect would be difficult to infer from the relatively small change in feed side pressure drop.

Fig. 7 shows the mean velocity in the feed channel region as a function of spiral position (odd and even spiral numbers refer to the two intertwined membrane sheets respectively – numbered with spiral 1 adjacent to the permeate channel) for the clean and lightly fouled velocity measurements – there are 14 spirals in total. The upper and lower bars indicate the standard deviation of the velocity distribution for the respective spiral. The clean membrane module has approximately constant velocity as a function of spiral number with the standard deviation being relative consistent for the three axial locations monitored.

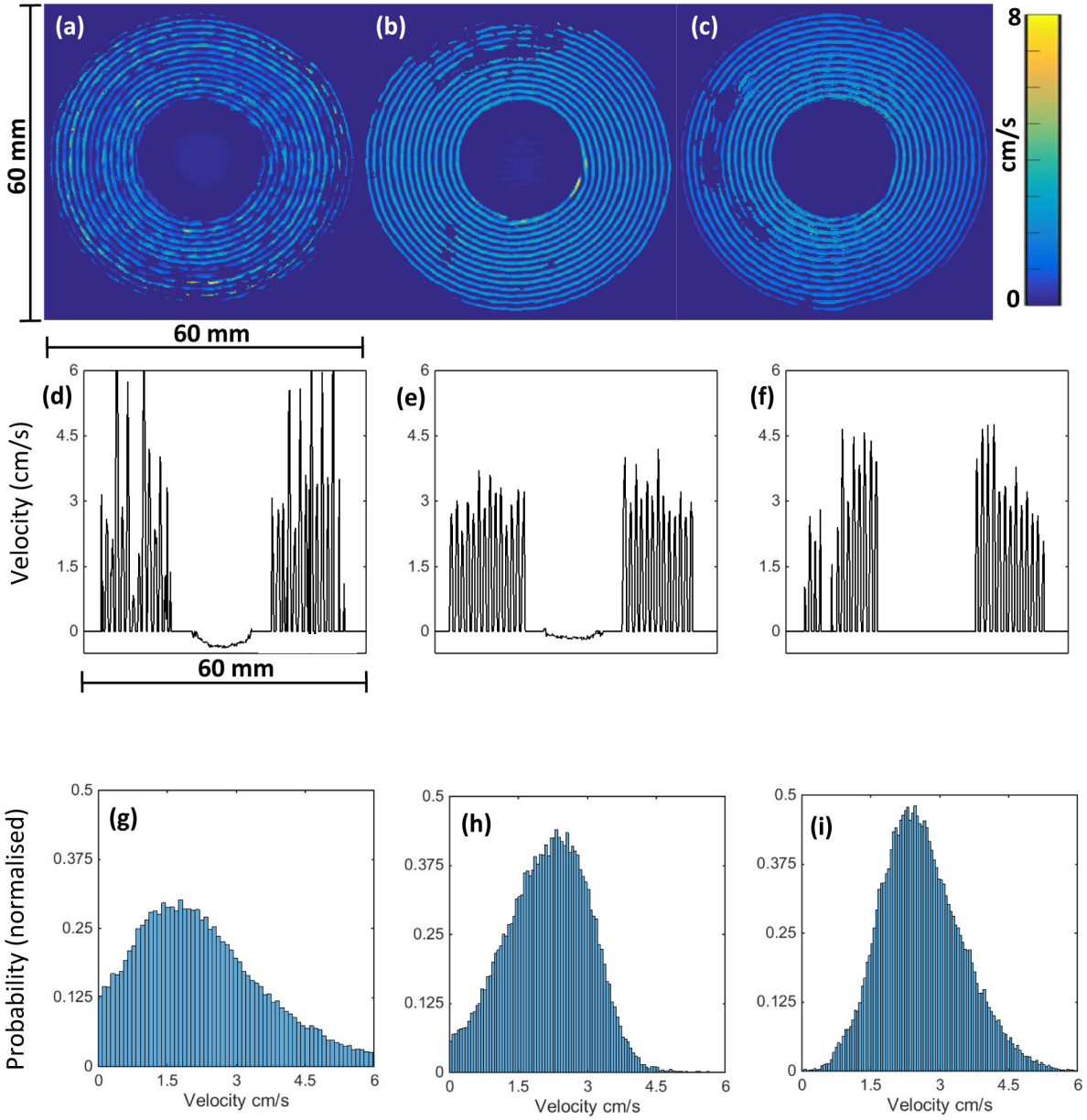

Fig. 5. Membrane exposed to a light fouling load (3.25 mg/l alginate in the whole system). Light fouling load membrane velocity images at (a) inlet, (b) middle and (c) outlet regions of membrane module. Velocity profiles across the mid-section of the velocity images at (d) inlet, (e) middle and (f) outlet region. Histograms of the velocity distributions for lightly fouled membrane at (g) inlet, (h) middle and (i) outlet region for the feed channels.

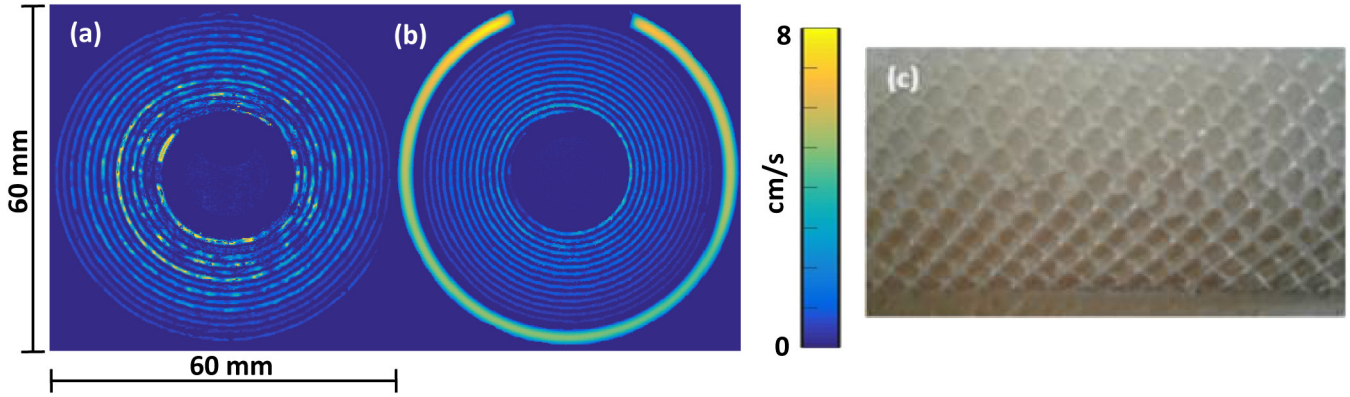

Fig. 6. Membrane exposed to a heavy fouling load (75 mg/l of alginate in the whole system). Velocity images are shown for (a) the entry region and (b) the exit region. Clear by-passing of the membrane module is evident in (b). (c) Shows an example membrane autopsy photo of the alginate gel on the feed spacer.

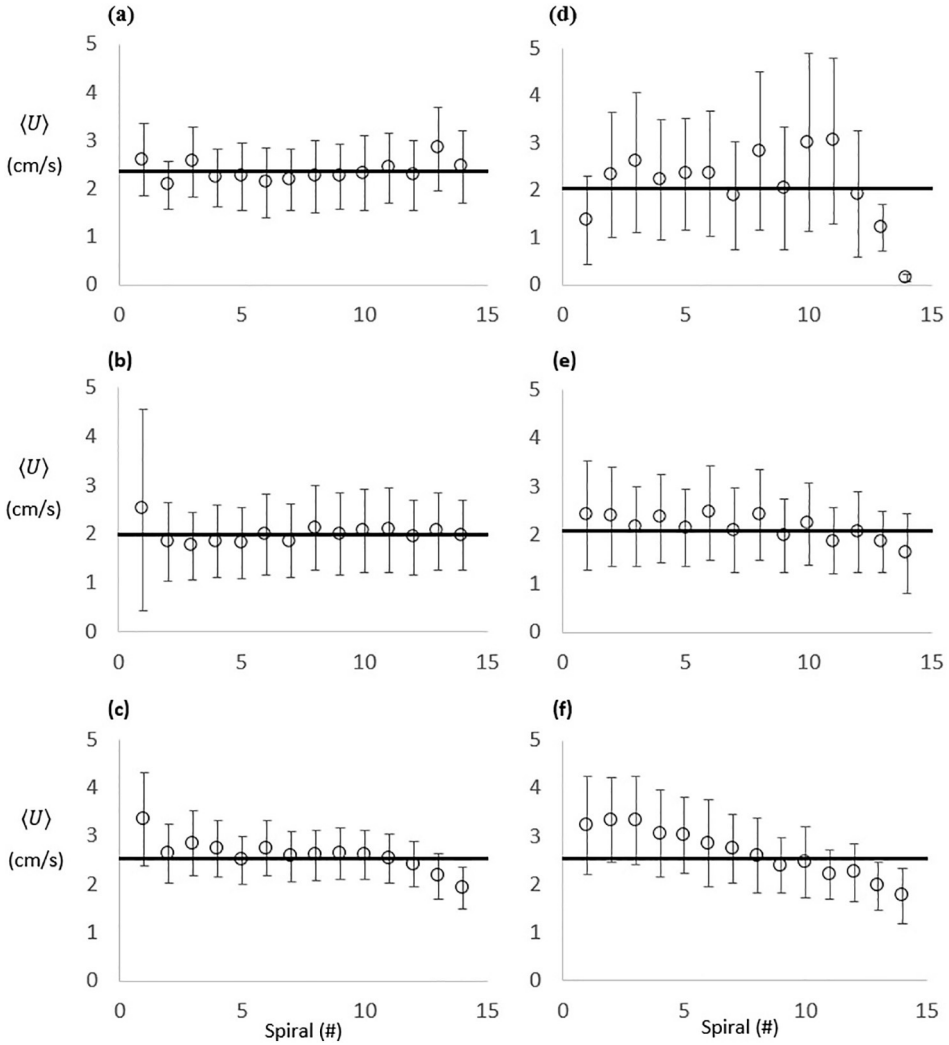

Fig. 7. Shows the average velocity (⟨U⟩ (cm/s)) in each spiral ($^{\#}$1 to $^{\#}$14, numbered from the permeate channel)) for the un-fouled and the lightly fouled membranes (a-c: un-fouled and d-f: lightly fouled). The upper and lower bars are the standard deviation of the velocity distribution, not the error, obtained for each spiral. (a, d): Inlet region; (b, e): Middle region; (c, f): Outlet region. Solid line indicates the cumulative average velocity across all spirals.

In contrast, the lightly fouled membrane module presents more variation in mean velocity and significantly more variation in the velocity standard deviation (particularly with respect to the inlet region). With respect to the inlet position the fluid mean velocity oscillation between spirals (and hence membrane sheets) is evident albeit more subtly than is visually evident in Fig. 5(a). For the middle region there is strong similarity between the un-fouled and lightly fouled membranes, whilst in the exit section of the membrane module, a clear trend of decreasing mean velocity with increasing spiral number is distinctly evident. This indicates that there is a preferential flow towards the inner side of the spiral assembly due to fouling. The observations of decreasing flow with radial position (Fig. 7f) in the fouled system is likely due to the module being more tightly bound in the outer regions (see Fig. 7c) which slightly lowers velocity. The higher surface area per unit volume encourages preferential fouling in this region which accentuates fouling there, therefore working as a feedback mechanism. These observations require more systematic study of the relationships between membrane module construction and the effect of foulants, to further elucidate any enhanced sensitivity to fouling.

The results presented in this work provide novel insights into the detailed fluid flow field inside an operating spiral wound reverse osmosis membrane module as a function of fouling extent. Such data should prove valuable to attempts to both numerically model flow processes inside this complex geometry membrane modules as well as the potential effect of any system modifications to improve the performance of seawater and brackish water desalination membrane systems, making these water treatment processes for drinking water and industrial water production cheaper, more reliable, and more environmentally friendly. Myriad CFD simulations across various spacer geometries and flow conditions exist in the literature [51–54], however the current experimental work on the full flow field within an operating SWM module experiencing fouling, has due to computational difficulties only been partially addressed (e.g. predominantly on a spacer-by-spacer & flat-sheet level) by CFD modelling to-date [54,55]. We therefore intend that the current results may aid in future developments of CFD modelling of the features exemplified in the current work.

4. Conclusions

In this study, heterogeneous flow channelling in the feed spacer channel regions are observed using cross-sectional non-invasive MRI velocity images, due to the addition of a small amount of alginate (3.25 mg/l) to the water flow loop. Flow heterogeneity is greatest near the entry to the spiral wound membrane module with alginate fouling confirmed by destructive system autopsy. Generally fouling also results in preferential flow towards the inner side of the spiral assembly whilst clear differences in velocity (and by inference fouling extent) was evident between the two membrane sheets and associated feed spacers

from which the module was assembled. This collective fouling resulted in a subtle increase in feed channel pressure drop and a distinct reduction in permeate production. After further addition of alginate (75 mg/l system concentration of alginate) the membrane module outer brine seal was observed to fail, causing water flow to by-pass the membrane module. Future research will aim at operating membrane modules at both higher velocities and higher pressures, mimicking typical process conditions for practise production of industrial and drinking water, exploring the image contrast caused by the accumulating alginate and a wider range of potential feed water foulants.

CRediT authorship contribution statement

Nicholas W. Bristow: Methodology, Software, Validation, Formal analysis, Investigation, Writing - original draft, Visualization. **Sarah J. Vogt**: Methodology, Software, Formal analysis, Investigation, Writing - review & editing, Supervision. **Keelan T. O'Neill**: Software, Formal analysis, Writing - original draft. **Johannes S. Vrouwenvelder**: Conceptualization, Writing - review & editing, Supervision. **Michael L. Johns**: Conceptualization, Methodology, Writing - review & editing, Supervision, Project administration. **Einar O. Fridjonsson**: Conceptualization, Methodology, Formal analysis, Investigation, Writing - review & editing, Visualization, Supervision, Project administration.

Acknowledgements

The authors acknowledge Mr. Ryuta Ujihara's assistance setting up the flow loop used in this work for the MRI measurements. The authors acknowledge Mr. David Amm's assistance and expertise in design and fabrication of the various custom parts used in this work. The authors acknowledge Dr. Kirk Feindel, the Centre for Microscopy and Characterisation and analysis (CMCA) at UWA and the Australian National Imaging Facility (NIF) for use of 9.4T MRI instrument used in this work.

Declaration of competing interest

The authors declare that they have no known competing financial interests or personal relationships that could have appeared to influence the work reported in this paper.

References

[1] U.N. Water, Coping with water scarcity: Challenge of the twenty-first century, 2007 World Water Day, United Nations - Food & Agriculture Organisation, 2007, p. 29.
[2] L.F. Greenlee, D.F. Lawler, B.D. Freeman, B. Marrot, P. Moulin, Reverse osmosis desalination: water sources, technology, and today's challenges, Water Res. 43 (2009) 2317–2348.
[3] W. Lawler, Z. Bradford-Hartke, M.J. Cran, M. Duke, G. Leslie, B.P. Ladewig, P. Le-Clech, Towards new opportunities for reuse, recycling and disposal of used reverse osmosis membranes, Desalination 299 (2012) 103–112.
[4] K. Tasaka, T. Katsura, H. Iwahori, Y. Kamiyama, Analysis of RO elements operated at more than 80 plants in Japan, Desalination 96 (1994) 259–272.
[5] H.F. Ridgway, H.C. Flemming, Membrane biofouling in water treatment membrane processes, J. Membr. Sci. 175 (1996) 61–73.
[6] E.M. Vrijenhoek, S. Hong, M. Elimelech, Influence of membrane surface properties on initial rate of colloidal fouling of reverse osmosis and nanofiltration membranes, J. Membr. Sci. 188 (2001) 115–128.
[7] M.A. Shannon, P.W. Bohn, M. Elimelech, J.G. Georgiadis, B.J. Mariñas, A.M. Mayes, Science and technology for water purification in the coming decades, Nature 452 (2008) 301.
[8] J.S. Vrouwenvelder, S.A. Manolarakis, J.P. van der Hoek, J.A.M. van Paassen, W.G.J. van der Meer, J.M.C. van Agtmaal, H.D.M. Prummel, J.C. Kruithof, M.C.M. van Loosdrecht, Quantitative biofouling diagnosis in full scale nanofiltration and reverse osmosis installations, Water Res. 42 (2008) 4856–4868.
[9] H.F. Ridgway, Biological Fouling of Separation Membranes Used in Water Treatment Applications, AWWA Research Foundation, 2003.
[10] J.S. Vrouwenvelder, M.C.M. van Loosdrecht, J.C. Kruithof, Early warning of biofouling in spiral wound nanofiltration and reverse osmosis membranes, Desalination 265 (2011) 206–212.
[11] J.S. Vrouwenvelder, J.A.M. van Paassen, L.P. Wessels, A.F. van Dam, S.M. Bakker, The membrane fouling simulator: a practical tool for fouling prediction and control, J. Membr. Sci. 281 (2006) 316–324.
[12] M.F.A. Goosen, S.S. Sablani, H. Al-Hinai, S. Al-Obeidani, R. Al-Belushi, D. Jackson, Fouling of reverse osmosis and ultrafiltration membranes: a critical review, Sep. Sci. Technol. 39 (2005) 2261–2297.
[13] R.A. Al-Juboori, T. Yusaf, Biofouling in RO system: mechanisms, monitoring and controlling, Desalination 302 (2012) 1–23.
[14] H.C. Flemming, G. Schaule, T. Griebe, J. Schmitt, A. Tamachkiarowa, Biofouling—the Achilles heel of membrane processes, Desalination 113 (1997) 215–225.
[15] J.W. Costerton, Z. Lewandowski, D.E. Caldwell, D.R. Korber, H.M. Lappin-Scott, Microbial Biofilms, Annu. Rev. Microbiol. 49 (1995) 711–745.
[16] W. Guo, H.-H. Ngo, J. Li, A mini-review on membrane fouling, Bioresour. Technol. 122 (2012) 27–34.
[17] A. Matin, Z. Khan, S.M.J. Zaidi, M.C. Boyce, Biofouling in reverse osmosis membranes for seawater desalination: phenomena and prevention, Desalination 281 (2011) 1–16.
[18] S.J. Vogt, A.B. Sanderlin, J.D. Seymour, S.L. Codd, Permeability of a growing biofilm in a porous media fluid flow analyzed by magnetic resonance displacement-relaxation correlations, Biotechnol. Bioeng. 110 (2013) 1366–1375.
[19] J.S. Vrouwenvelder, M.C.M. Van Loosdrecht, J.C. Kruithof, A novel scenario for biofouling control of spiral wound membrane systems, Water Res. 45 (2011) 3890–3898.
[20] T.R.R. Pintelon, C. Picioreanu, M.C.M. van Loosdrecht, M.L. Johns, The effect of biofilm permeability on bio-clogging of porous media, Biotechnol. Bioeng. 109 (2012) 1031–1042.
[21] H.-C. Flemming, Reverse osmosis membrane biofouling, Exp. Thermal Fluid Sci. 14 (1997) 382–391.
[22] J.S. Vrouwenvelder, D.A. Graf von der Schulenburg, J.C. Kruithof, M.L. Johns, M.C. van Loosdrecht, Biofouling of spiral-wound nanofiltration and reverse osmosis membranes: a feed spacer problem, Water Res. 43 (2009) 583–594.
[23] Y. Marselina, P. Lifia, R.M. Le-Clech, V. Stuetz, Chen, Characterisation of membrane fouling deposition and removal by direct observation technique, J. Membr. Sci. 341 (2009) 163–171.
[24] T. Chilcott, A. Antony, H. Coster, G. Leslie, In situ characterization of fouling in reverse osmosis membranes using electrical impedance spectroscopy, J. Phys. Conf. Ser. 434 (2013) 12089.
[25] S. Lee, W.S. Ang, M. Elimelech, Fouling of reverse osmosis membranes by hydrophilic organic matter: implications for water reuse, Desalination 187 (2006) 313–321.
[26] P. van den Brink, F. Vergeldt, H. Van As, A. Zwijnenburg, H. Temmink, M.C.M. van Loosdrecht, Potential of mechanical cleaning of membranes from a membrane bioreactor, J. Membr. Sci. 429 (2013) 259–267.
[27] Y. Ye, P. Le Clech, V. Chen, A.G. Fane, B. Jefferson, Fouling mechanisms of alginate solutions as model extracellular polymeric substances, Desalination 175 (2005) 7–20.
[28] P. van den Brink, A. Zwijnenburg, G. Smith, H. Temmink, M. van Loosdrecht, Effect of free calcium concentration and ionic strength on alginate fouling in cross-flow membrane filtration, J. Membr. Sci. 345 (2009) 207–216.
[29] P.U. Berman, T, Transparent xopolymer Particles (TEP): an overlooked factor in the process of biofilm formation in aquatic environments, Nature Precedings 1 (2007).
[30] K.J. Farrell, Reduced membrane fouling potential by tailored fluid/structure interaction, Desalination and Water Purification Research and Development Program Report 143 (2008) 1–60.
[31] B.J. Pangrle, E.G. Walsh, S. Moore, D. DiBiasio, Investigation of fluid flow patterns in a hollow fiber module using magnetic resonance velocity imaging, Biotechnol. Tech. 3 (1989) 67–72.
[32] C.A. Heath, G. Belfort, B.E. Hammer, S.D. Mirer, J.M. Pimbley, Magnetic Resonance Imaging and Modeling of Flow in Hollow-Fiber Bioreactors, (1990).
[33] S. Yao, M. Costello, A.G. Fane, J.M. Pope, Non-invasive observation of flow profiles and polarisation layers in hollow fibre membrane filtration modules using NMR micro-imaging, J. Membr. Sci. 99 (1995) 207–216.
[34] J.M. Pope, S. Yao, A.G. Fane, Quantitative measurements of the concentration polarisation layer thickness in membrane filtration of oil-water emulsions using NMR micro-imaging, J. Membr. Sci. 118 (1996) 247–257.
[35] D. Airey, S. Yao, J. Wu, V. Chen, A.G. Fane, J.M. Pope, An investigation of concentration polarization phenomena in membrane filtration of colloidal silica suspensions by NMR micro-imaging, J. Membr. Sci. 145 (1998) 145–158.
[36] P.A. Hardy, C.K. Poh, Z.J. Liao, W.R. Clark, D.Y. Gao, The use of magnetic resonance imaging to measure the local ultrafiltration rate in hemodialyzers, J. Membr. Sci. 204 (2002) 195–205.
[37] S. Buetehorn, L. Utiu, M. Küppers, B. Blümich, T. Wintgens, M. Wessling, T. Melin, NMR imaging of local cumulative permeate flux and local cake growth in submerged microfiltration processes, J. Membr. Sci. 371 (2011) 52–64.
[38] P.Z. Çulfaz, S. Buetehorn, L. Utiu, M. Kueppers, B. Bluemich, T. Melin, M. Wessling, R.G.H. Lammertink, Fouling behavior of microstructured hollow Fiber membranes in dead-end filtrations: critical flux determination and NMR imaging of particle deposition, Langmuir 27 (2011) 1643–1652.
[39] X. Yang, E.O. Fridjonsson, M.L. Johns, R. Wang, A.G. Fane, A non-invasive study of flow dynamics in membrane distillation hollow fiber modules using low-field nuclear magnetic resonance imaging (MRI), J. Membr. Sci. 451 (2014) 46–54.
[40] F. Arndt, S. Schuhmann, G. Guthausen, S. Schütz, H. Nirschl, In situ MRI of alginate fouling and flow in ceramic hollow fiber membranes, J. Membr. Sci. 524 (2017) 691–699.
[41] N. Schork, S. Schuhmann, F. Arndt, S. Schütz, G. Guthausen, H. Nirschl, MRI investigations of filtration: fouling and cleaning processes, Microporous Mesoporous

Mater. 269 (2017) 60–64.
[42] D. Graf Von der Schulenburg, J.S. Vrouwenvelder, S.A. Creber, M.C.M. Van Loosdrecht, M.L. Johns, Nuclear magnetic resonance microscopy studies of membrane biofouling, J. Membr. Sci. 323 (2008) 37–44.
[43] S.A. Creber, J.S. Vrouwenvelder, M.C.M. van Loosdrecht, M.L. Johns, Chemical cleaning of biofouling in reverse osmosis membranes evaluated using magnetic resonance imaging, J. Membr. Sci. 362 (2010) 202–210.
[44] E.O. Fridjonsson, S.A. Creber, J.S. Vrouwenvelder, M.L. Johns, Magnetic resonance signal moment determination using the Earth's magnetic field, J. Magn. Reson. 252 (2015) 145–150.
[45] R. Ujihara, E. Fridjonsson, N. Bristow, S. Vogt, S. Bucs, J. Vrouwenvelder, M. Johns, Earth's field MRI for the non-invasive detection of fouling in spiral-wound membrane modules in pressure vessels during operation, Desalin. Water Treat. 135 (2018) 16–24.
[46] E. Fridjonsson, S. Vogt, J. Vrouwenvelder, M. Johns, Early non-destructive biofouling detection in spiral wound RO membranes using a mobile earth' s field NMR, J. Membr. Sci. 489 (2015) 227–236.
[47] J.M. Pope, S. Yao, Flow-selective pulse sequences, Magn. Reson. Imaging 11 (1993) 585–591.
[48] P. Xu, J.E. Drewes, C. Bellona, G. Amy, T.-U. Kim, M. Adam, T. Heberer, Rejection of emerging organic micropollutants in Nanofiltration–reverse osmosis membrane applications, Water Environment Research 77 (2005) 40–48.
[49] D.L. Separations, Filmtec Reverse Osmosis Membranes - Technical Manual in, Dow Liquid Separations, (2005).
[50] E.H. Lockwood, A Book of Curves, Cambridge University Press, 1967.
[51] S.S. Bucs, R.V. Linares, J.O. Marston, A.I. Radu, J.S. Vrouwenvelder, C. Picioreanu, Experimental and numerical characterization of the water flow in spacer-filled channels of spiral-wound membranes, Water Res. 87 (2015) 299–310.
[52] Y.-L. Li, K.-L. Tung, Y.-S. Chen, K.-J. Hwang, CFD analysis of the initial stages of particle deposition in spiral-wound membrane modules, Desalination 287 (2012) 200–208.
[53] V.A. Haaksman, A. Siddiqui, C. Schellenberg, J. Kidwell, J.S. Vrouwenvelder, C. Picioreanu, Characterization of feed channel spacer performance using geometries obtained by X-ray computed tomography, J. Membr. Sci. 522 (2017) 124–139.
[54] J.S. Vrouwenvelder, C. Picioreanu, J.C. Kruithof, M.C.M. Van Loosdrecht, Biofouling in spiral wound membrane systems: three-dimensional CFD model based evaluation of experimental data, J. Membr. Sci. 346 (2010) 71–85.
[55] A.J. Karabelas, M. Kostoglou, C.P. Koutsou, Modeling of spiral wound membrane desalination modules and plants–review and research priorities, Desalination 356 (2015) 165–186.